Research Article | Vol. 30, No. 2 / 17 Jan 2022 / Optics Express 2768

Optics EXPRESS

Interpreting light guidance in antiresonant and photonic bandgap waveguides and fibers by light scattering: analytical model and ultra-low guidance

GUANGRUI LI,[1] RON FATOBENE ANDO,[2] MATTHIAS ZEISBERGER,[2] THOMAS WEISS,[3] AND MARKUS A. SCHMIDT[2,4,5,*]

[1] *Friedrich Schiller University Jena, Max-Wien-Platz 1, 07743 Jena, Germany*
[2] *Leibniz Institute of Photonic Technology, Albert-Einstein-Str. 9, 07745 Jena, Germany*
[3] *Institute of Physics, University of Graz, and NAWI Graz, Universitätsplatz 5, 8010 Graz, Austria*
[4] *Abbe Center of Photonics, Friedrich Schiller University Jena, Max-Wien-Platz 1, 07743 Jena, Germany*
[5] *Otto Schott Institute of Materials Research, Fraunhoferstr. 6, 07743 Jena, Germany*
[*] *markus.schmidt@leibniz-ipht.de*

Abstract: Here, we introduce a quasi-analytic model that allows studying mode formation in low refractive index core waveguides through solely focusing on the cladding properties. The model isolates the reflection properties of the cladding from the modes via correlating the complex amplitude reflection coefficient of the cladding to the complex effective index of the fundamental core mode. The relevance and validity of the model are demonstrated by considering a single-ring anti-resonant fiber, revealing unexpected situations of exceptionally low loss. Our model explains mode formation by light scattering, which conceptually provides deep insights into the relevant physics.

1. Introduction

Waveguides and in particular optical fibers with low refractive index (RI) cores guide light through sophisticated optical effects and require well-designed microstructured claddings for efficiently confining the light, having led to application in important fields such as life-science [1], nonlinear frequency conversion [2] or quantum technology [3]. Due to the lack of total internal reflection, the modes of such waveguides continuously dissipate energy along the transverse directions, i.e. are intrinsically leaky [4], demanding precise cladding design to minimize losses. The mechanisms used to guide light include (i) the antiresonance (AR) effect [5,6], (ii) photonic bandgap (PBG) guidance [7,8] and (iii) inhibited coupling (IC) [9,10].

From the geometry perspective, complex cladding geometries that can include hundreds of high RI cylinders arranged in predefined lattices [11–13] or waveguides with simplified cladding structures including pixelated Bragg fiber [14], tube lattice AR fibers [15], single- and dual-ring light cage [16] have recently attracted significant attention. These systems are proven to be efficient solutions for high-quality optical beam delivery and low-loss guidance, overall becoming a rapidly growing research field. All these structures have in common that analyzing the relevant guidance mechanism and precise structure design remain key challenges due to complex and in many situations spatially extended microstructures.

The most widely used method to analyze low-RI core waveguides relies on full numerical modeling, i.e., on searching for Eigensolutions (i.e. modes) of the entire waveguide system in the frequency domain. Here, uncovering the details of the reflective properties of the cladding and thus performance optimization are challenging as the contribution of the microstructured cladding to the modal properties cannot be isolated. In addition, full numerical modelling for large core dimensions, which holds for the majority of fiber waveguides, requires excessive

#445884 https://doi.org/10.1364/OE.445884
Journal © 2022 Received 13 Oct 2021; revised 6 Dec 2021; accepted 9 Dec 2021; published 12 Jan 2022

simulation time, as both the finely structured cladding and the large core have to be discretized simultaneously.

Various approximate models were developed to address this issue, yielding (semi-)analytical expressions for dispersion and loss (i.e. complex effective indices) of the core modes. Specifically, models for single-ring or multi-layer AR fibers [17–21] have been reported and extended towards tube lattice AR fibers [22–24]. For instance, the anti-resonant reflecting optical waveguide (ARROW) model can be used for estimating the wavelengths of minimal transmission [25], while a more sophisticated model that is based on a Floquet-Bloch approach neglects the core mode and investigates the photonic band formation [26–28].

Regardless of the cladding structures, light guidance in waveguides can be understood on the basis of waves [29]: Here, mode formation results from the interference of two counter-zigzagging waves that are reflected at the core-cladding boundary. The core modes exist when the accumulated phase shift across the core plus the reflection-induced phase change leads to constructive interference [30,31]. This physical picture highlights the relevance of the cladding and suggests that understanding the cladding's scattering properties is essential.

In previous works, we have introduced a reflection-based model that approximates a circular cladding by its planar counterpart, leading to analytic expressions for the complex effective mode index for a hypothetical annulus type AR fiber [21] and allowing for designing a water-core fiber with an all-solid cladding [32]. In case the core diameter is much larger than the operation wavelength, the cladding curvature can be neglected, and the field can be locally approximated as a single plane wave reflecting at the microstructured cladding. These previous works show that the dispersion and loss of the core modes can be obtained analytically in case the reflection properties of the cladding are known. However, the specific correlation between the transmission and reflection coefficients of the cladding and the modal parameters were not explicitly derived, thus having strongly limited the applicability of the wave model to specific waveguide scenarios.

In this work, we address this issue and introduce a general quasi-analytical model that unambiguously correlates the complex transmission and reflection properties of a cladding with the modal properties. This model thus makes it possible to explore and in particular to optimize the properties of the cladding independently of modal calculations. The advantageous properties of the model are demonstrated using the single-ring fiber as an example, where extremely low losses were found for certain geometric configurations.

2. Details of the reflection model

2.1. Derivation of model

The fundamental working principle of our model relies on correlating the modal properties (here complex effective mode index n_{eff}) of the waveguide to the complex amplitude transmission/reflection coefficients of the corresponding approximated planar cladding structure (complex single-interface amplitude reflection coefficient: r). In the following, we introduce our reflection-based model and demonstrate its relevance on the example of simulating the fundamental mode (FM) of an all-solid single ring AR fiber. The geometry (Fig. 1(a)) is defined by an array of circularly arranged high RI dielectric cylinders (RI: $n_s = \Delta n + n_c$ ($\Delta n = 0.02$), diameter: d, center-to-center spacing (pitch): Λ) embedded in silica (RI: $n_c = n_{\mathrm{silica}}$, [33]) encircling a large central core (core diameter (boundary-to-boundary): D_c). Here a large core diameter refers to the situation that the core radius R is large compared to the wavelength λ ($R \gg \lambda$) leading to a small angle between the rays and the waveguide axis or the surface of the cylinders. Note that this geometry was deliberately chosen to resemble the commonly considered situation of a PBG fiber, consisting of GeO_2-doped strands located in a silica background [34]. This particular choice was made to present the model in an illustrative way, although the applicability of the model is by no means limited to this example.

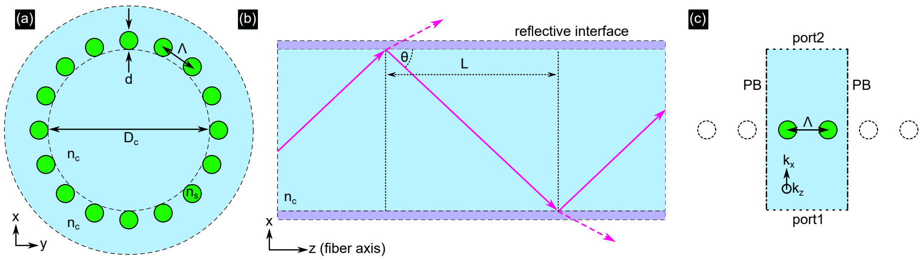

Fig. 1. (a) Sketch of the single-ring AR fiber used here to demonstrate the properties of our model. (b) The concept of the quasi-analytic model with key parameters: n_c, θ and L. The pink lines refer to the waves zigzagging inside the waveguide core. (c) Geometry used to calculate the reflection and transmission properties of the corresponding planar structure.

In the case of a cylindrical core surrounded by a perfectly reflecting core-cladding interface, constructive interference leads to guided modes in the core in the form of Bessel solutions. The phase of light resulting from the transverse confinement is given by the roots of the Bessel function: $j_{lm} = \kappa R$ (transverse component of the wave vector in the core: κ, mth root of the Bessel function J_l: j_{lm}, core radius: $R = D_c/2$). Therefore, the transverse component of the wave vector of the fundamental core mode (FM) can be analytically expressed as:

$$\kappa = \frac{j_{01}}{R}. \tag{1}$$

where j_{01} is the first root of the zero-order Bessel function.

For the sake of simplicity, we consider guidance of the light in a fiber with large core, which allows to assume that the light wave gets reflected and transmitted at a corresponding planar boundary. The bouncing angle θ and the longitudinal distance between two reflections ($L = L(\theta)$ in Fig.1 (a)) can be expressed as:

$$\theta = \arcsin\frac{\kappa}{k} \approx \frac{\kappa}{k} = \frac{j_{01}}{kR}, \quad L = \frac{2R}{\tan(\theta)} \approx \frac{2R}{\theta}. \tag{2}$$

with the wave vector $k = k_0 n_c$ (n_c: core index, $k_0 = 2\pi/\lambda_0$: vacuum wave vector (λ_0: vacuum wavelength)). Note that the approximation used in Eq. (2) is valid for the case when the propagation constant $\beta \gg \kappa$, which is true for a large core fiber, especially for the low-order modes.

The complex reflection and transmission behavior at a planar resonant cladding induce an additional phase change and loss that need to be accounted for. Here, we calculate the dispersion (real part of effective mode index Re(n_{eff})) and loss γ of the modes of such leaky waveguide analytically using the complex single-interface amplitude reflection coefficient r obtained from planar model simulations (Fig. 2(b)).

Assuming that the microstructured cladding is essentially a perturbed perfectly reflecting core-cladding interface, the dispersion of the FM in a leaky case can be expressed as follows:

$$\text{Re}(n_{\text{eff}}) = \sqrt{n_c^2 - \left(\frac{j_{01}}{k_0 R}\right)^2} + \frac{\Delta\Phi_r(\theta)}{k_0 L}. \tag{3}$$

where $\Delta\Phi_r(\theta) = \arg(r(\theta))$ is the phase change per reflection at bouncing angle θ (the latter is analytically defined in Eq. (2). Equation (3) nicely illustrates that the dispersion properties of a leaky waveguide with resonant cladding depends, in addition to perfect reflection (term under the square root), on the phase change of the single reflection event (most right-handed term). Using

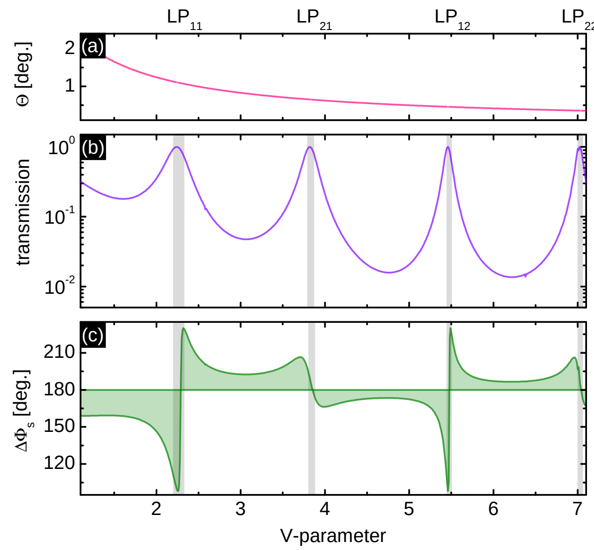

Fig. 2. Dependence of the various model-related parameters on the waveguide parameter V (note that here V is varied by changing d) of the single-ring AR fiber shown in Fig. 1(a) (simulation parameters can be found in the main text). (a) Bouncing angle θ for the fundamental mode (HE_{11}-mode). (b) Transmission at port2 of the planar geometry (Fig. 1(c)). (c) Corresponding phase difference between the forward scattered field by the structure and the incident field $\Delta\Phi_s$. The gray areas in (b) and (c) and the labels on the top of (a) refer to the LP-resonances (i.e., cut-offs) inside the cylinders.

the bouncing-angle dependent intensity transmission coefficient ($T = T(\theta)$) and the distance between two reflections ($L = L(\theta)$), the loss of the FM can then be described as:

$$\gamma[\text{dB/m}] = -10\frac{\log_{10}(1 - T(\theta)))}{L(\theta)} \approx 4.34294\frac{T(\theta)}{L(\theta)} \approx 0.8311\frac{T(\theta)\lambda_0}{n_c R^2} \quad \text{for,} \ T \ll 1, \tag{4}$$

showing that, with approximation for low loss ($T \ll 1$), the loss is proportional to the power transmission coefficient of the single interface T.

2.2. Verification of the model

The corresponding numerical planar model used to determine optical properties of the approximated planar structure consists of a periodic arrangement of cylinders using a two cylinder segment of the AR fiber, including periodic boundary (PB) conditions (Fig. 1(c)). Two ports were defined to receive the reflection and transmission properties of the structure.

For the following simulations we choose the number of cylinders $N = 16$, $d/\Lambda = 0.50$ and the operation wavelength $\lambda = 1\mu\text{m}$. Here, we vary the V parameter $V = \pi d(n_s^2 - n_c^2)^{1/2}/\lambda$ by changing the diameter of the cylinders d while keeping λ fixed. Note that we have d/Λ fixed, therefore, while d increases, D_c and R increase accordingly and the angle θ also changes according to Eq. (2). To illustrate this effect, the angle θ of the FM is plotted in Fig. 2(a), showing considerable small values supporting the approximation used in Eq. (2). Note that for this example, we used sin and tan in the calculation for θ.

The small index contrast ($\Delta n = 0.02$) between cylinders and background results in a polarization independent reflection, as it can be shown for the reflection at a single interface with the Fresnel equation. Therefore, we can employ a single plane wave (transverse-magnetic (TM) polarization is used here, transverse-electric (TE) will be the same) as the incident field from port1.

The distribution of the power transmission coefficient T for various V-parameter, calculated at port2 in the planar model (Fig. 2(b)) shows periodically appearing maxima corresponding to the resonances in the cladding. To illustrate this qualitatively, Fig. 2(c) shows the related phase difference between the incident and forward scattered electric fields $\Delta\Phi_s$. Here, the domains of low transmission are associated with phase differences close to 180°, demonstrating the importance of destructive interference in the microstructured cladding for achieving low-loss values.

In Fig. 3 we show the dispersion and loss of the FM of the single-ring AR fiber obtained by the equations above using the planar reflection calculations (green solid lines, Eqs. (3)–(4)) in comparison to full numerical modal calculation with the finite element method (FEM) for the circular waveguide structure (purple dots, structure shown in Fig. 1(a)). Although the angles used in the reflection-based model were approximated by those of the corresponding perfectly reflecting waveguide and no further assumptions were considered, the results of the reflection model excellently match the dispersion and loss of the large-core AR fiber. Only slight discrepancies are visible at small V values, which can be attributed to the larger bouncing angles θ making the assumptions of the model more critical.

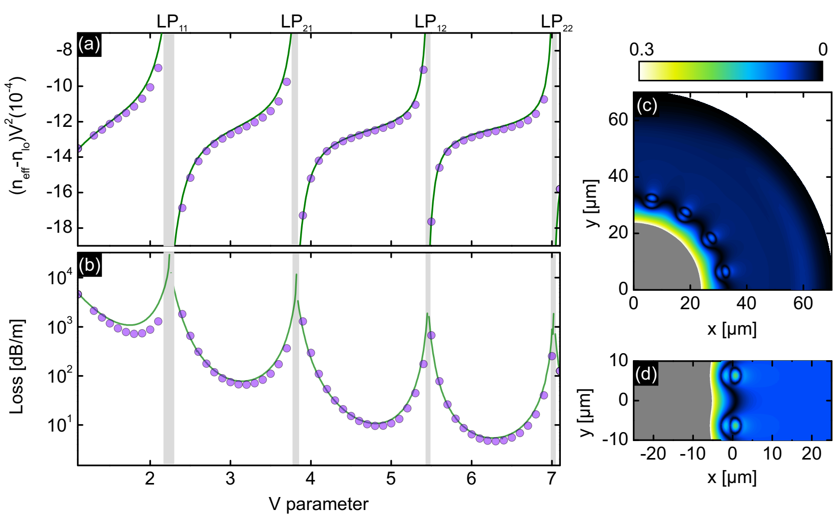

Fig. 3. Comparison of the calculated waveguide dispersion of the FM of the single-ring AR fiber considered in Fig. 2 using the reflection-based model (green solid line) and full numerical simulations (purple dots, Finite-Element modelling). Note that the V-parameter is varied by changing the cylinder diameter d. (a) Dispersion of phase index (here the normalized relative phase index is used and $n_{lo} = n_{silica}(\lambda = 1\ \mu m)$). The labels on the top of the plot indicate the cylinder modes that anti-cross with the core mode, i.e., identify the respective resonance. (b) Modal loss (in units of dB/m). The gray bars indicate the resonances of the cladding. Normalized electric field distributions (norm of E-field) at an example waveguide parameter of $V = 4.81$ are shown on the right side ((c): modal simulations, (d): planar reflection model). Note that the intensity values shown are cropped at high values to make the characteristic features of the field patterns visible.

The spatial distribution of the electric fields (norm of E-field $|\mathbf{E}|^2$) clearly demonstrates the correspondence between mode field calculation (Fig. 3(c)) and the reflection-based model (Fig. 3(d)). Despite the simplification of the incident field being a single TM-polarized plane wave, the excited field in the cylinders, i.e. resonances, of the planar model is consistent with that of the modal calculation.

3. Results

3.1. All-solid single-ring AR fibers with identical cylinders

The capabilities of the model are demonstrated in the following by a large-scale parameter sweep of the modal loss of the FM for the all-solid single-ring AR fiber introduced in Fig. 1 (Fig. 4). Specifically, the study is concentrated on the V-parameter interval between the second and third resonance (LP_{21}- and LP_{12}-mode) of the cladding ($3.83<V<5.52$) and extends the calculation of Fig. 3 towards geometry-related dimension that refers to changing the d/Λ ratio (Λ is changed, d is fixed), leading to the loss map shown in Fig. 4(a). Remarkably, this map reveals regions of extraordinary low loss ($\gamma<10^{-4}$dB/m) for combinations of specific parameters. For a selected geometry (i.e. selected combinations of pitch and strand diameter (d/Λ = 0.3, horizontal dashed red line in Fig. 4(a)) the results of the model are compared with those from full numerical calculations (Fig. 4(b)), revealing a good match and therefore the applicability of the model also in situation of a strong susceptibility of the modal loss on the various parameters.

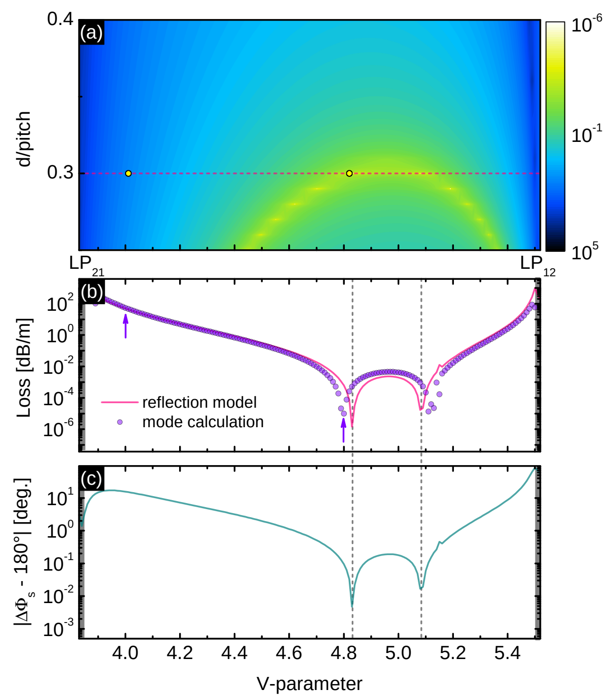

Fig. 4. (a) Loss of the fundamental core mode as a function of d/Λ (Λ is changed, d is fixed) and V-parameter (d is changed) for the all-solid single-ring AR fiber (parameter defined in the main text) between the LP_{21} and LP_{12} resonances. The color scale indicates the loss level in units of dB/m. The yellow dots refer to the configurations of the simulated fields shown in Fig. 5. The LP-labels refer to the resonances (abscissa labels also apply to (b) and (c)). (b) Comparison of the loss obtained from the reflection-based model (red line) and full numerical simulations (circular waveguide, purple dots) for a geometry that is defined by d/Λ = 0.3 (horizontal dashed red line in (a)). The two arrows indicate the configuration of the simulated fields shown in Fig. 5. (c) The corresponding relative absolute phase difference between the forward scattered and incident field $\Delta\Phi = |\Delta\Phi_s - 180°|$. The gray color bars in (b) and (c) indicate the resonances of the cladding.

In accordance with the discussion of the previous chapter, the corresponding relative absolute phase difference between the forward scattered field and the incident field $\Delta\Phi = |\Delta\Phi_s - 180°|$

Optics EXPRESS

is shown in Fig. 4(c). The same tendency as the loss distribution (Fig. 4(b)) is found, with $\Delta\Phi$ being close to 0° at the V parameters of the lowest loss, again emphasizing the relevance of this parameter within the context of minimize waveguide losses.

To demonstrate the relevance of $\Delta\Phi$, the z-component of the electric fields for the V parameters labeled with two arrows in Fig. 4(b) are shown in Fig. 5. In the case of a very low phase difference ($\Delta\Phi<(10^{-2})°$ at $V = 4.81$), destructive interference behind the structure ($y>0$) is clearly visible, leading to very low loss. This situation is different for $V = 4$, showing significant power transmission through the chain of cylinders. The results clearly reveal that the coupling between the modes of the cylinders is essential (Λ was changed in Fig. 4(a)), as the scattering from a single isolated cylinder does not show such low-loss behavior.

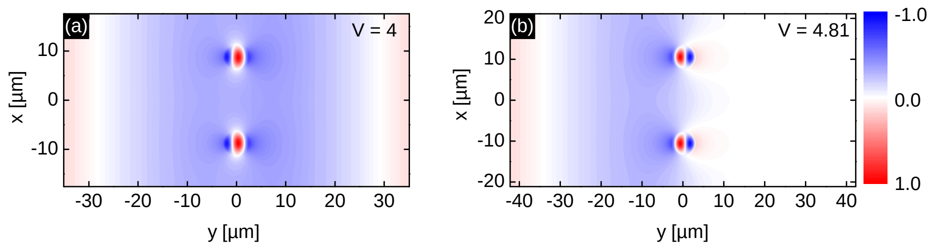

Fig. 5. Spatial distribution of the z-component of E-field plotted at the V-parameters labeled by arrows in Fig. 4(b). The fields are normalized to their maximum value and are rescaled to the range [0,1]. (a) $V = 4$; (b) $V = 4.81$.

3.2. All-solid single-ring AR fiber with alternating cylinders

A further reduction of the modal losses through modifying the geometry, i.e. to minimize $\Delta\Phi$, requires an additional degree of freedom as the geometry with identical cylinders is limited in terms of potential structural variations. For the single-ring AR fiber discussed here, a chain of cylinders with alternating diameters and identical RIs (Fig. 6(a)) is proposed in the context of this study, representing a promising approach as recently demonstrated [35] and a principally implementable extension of the discussed waveguide structures. Note that the planar reflection-based model contains one period of the diameter-modified structure (Fig. 6(b)).

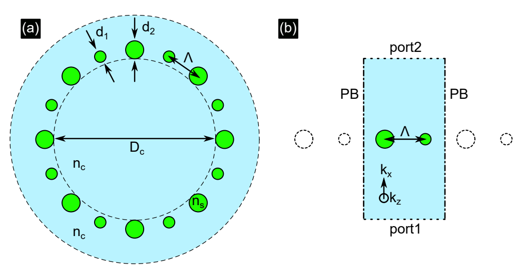

Fig. 6. (a) Sketch of the diameter-modified all-solid single-ring AR fiber and (b) the corresponding approximated planar model used to obtain the reflection properties of the cladding.

In the following, the modal loss is calculated as a function of the diameters of adjacent cylinders, while the pitch is fixed in accordance to the configuration giving the lowest loss in the previous study (at $V = 4.81$ and pitch $\Lambda = 1.2669\,\mu$m). Therefore, the resulting loss map includes V_1 and V_2 as varying parameters ($V_1 = \pi d_1(n_s^2 - n_c^2)^{1/2}/\lambda$, $V_2 = \pi d_2(n_s^2 - n_c^2)^{1/2}/\lambda$) and is shown in Fig. 7.

Optics EXPRESS

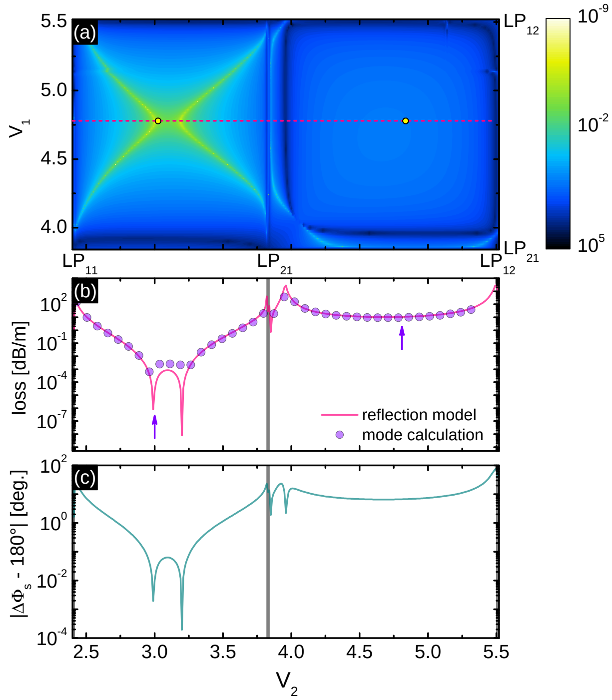

Fig. 7. (a) Map showing the modal loss of the modified cylinder structure as a function of V_1 and V_2 (d_1 and d_2 are varied, other parameters are fixed) for the diameter-modified all-solid single-ring AR fiber (N = 16, Λ = 1.2669 μm, λ = 1 μm, $n_c = n_{\text{silica}}$, $n_s = n_c + 0.02$). The two yellow dots refer to the configurations of the field plots shown in Fig. 8. The LP-labels refer to the resonances (abscissa labels also apply to (b) and (c)). (b) Modal loss as a function of V_2 for a constant value of V_1 (red dashed red line in (a), V_1 = 4.81, reflection-based model: pink, full numerical simulations: purple dots). (c) Corresponding relative absolute phase difference $\Delta\Phi$. The gray bars in (b) and (c) indicate the resonances of the cladding.

Here it is important to mention that the loss map (Fig. 7(a)) refers to two different regimes regarding V_1 and V_2: For the left part of the loss map (V_2<3.832) V_1 has values in-between the second and third resonances (LP_{21} and LP_{12}), while V_2 lies within the region between the first and second resonances (LP_{11} and LP_{21}). For the right side of the map (V_2>3.832), in contrast, both V_1 and V_2 are located in the domain between the second and third resonances (LP_{21} and LP_{12}). Here it is interesting to observe that the loss properties are different in these two cases: When neighboring cylinders refer to V parameters in different PBGs (left part), exceptionally loss as small as $\gamma \leq 10^{-7}$ dB/m appears for certain combination of parameters.

The plot in Fig. 7(b) shows the loss at V_1 = 4.81 (cut-line in Fig.7(a)) calculated from the reflection-based model (red line) and from the full numerical modal simulations (purple dots), again demonstrating the good match. The plot in Fig. 7(c) shows the corresponding relative phase difference $\Delta\Phi$, which is highly consistent with the loss trend in Fig.7(b) and, in accordance with the structure with constant cylinder diameter, is very close to 0° at the configurations yielding ultralow loss.

To reveal that destructive interference is essential for the appearance of the very low-loss values, Fig. 8 show the electric field distributions for the case of identical (a,c) and alternating cylinders (b,d) (Note that the two cases correspond to the configurations indicated by yellow dots and arrows in Figs. 7(a) and (b)). It is obvious that in contrast to identical cylinders, the excited fields in the modified cylinders are of different order and the coupling of the excited resonances leads to efficient destructive interference. The electric field distribution along the cut-line through the identical cylinders (Fig. 8(c)) confirms that behavior, while for the alternating cylinder situation (Fig. 8(d)), the electric field through the smaller cylinder exhibits one node less compared to the bigger cylinder, enabling very effective destructive interference.

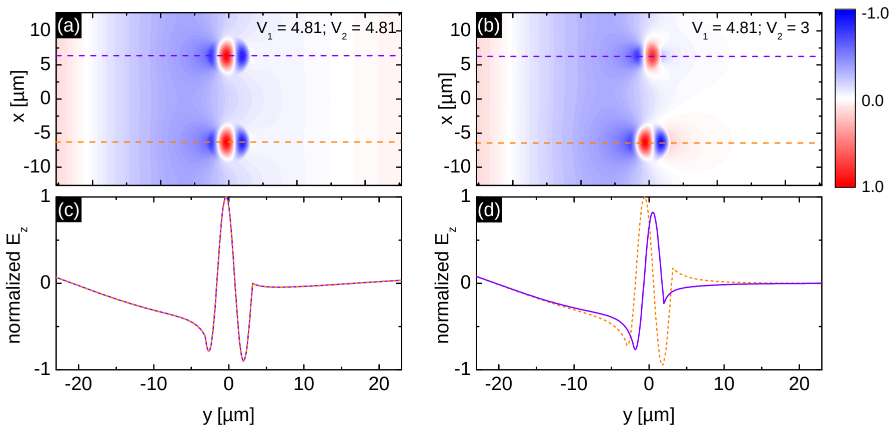

Fig. 8. Spatial distributions of the normalized rescaled z-components of electric fields for the configurations labeled by the yellow dots in Fig. 7(a) (the arrows in Fig. 7(b)). The lower plots refer to the distributions at the horizontal cut-lines that go through the centers of the individual cylinder (indicated by the dashed lines): (a,c) identical diameter configuration ($V_1 = V_2 = 4.81$). (b,d) ultralow-loss configuration ($V_1 = 4.81, V_2 = 3$).

4. Discussion

The interpretation of the guiding mechanism and the related losses in the context of waves being scattered at a core/cladding interface yields a clear correlation of losses and properties of the cladding, thus being highly useful to understand the occurrence of low loss domains. While the core field is a superposition of an outgoing wave and the backward scattered fields, the field in the outer medium results from the superposition of the forward scattered waves from the cylinders. Here, each cylinder can show an anti-resonant behavior at certain values of the V parameter, leading to a minimum in the forward scattering, i.e. to a minimum in the losses of the guided mode. Here, using two different cylinder diameters allows obtaining forward scattered waves with different phases, which can be tuned relative to each other to improve the destructive interference ($\Delta\Phi \approx 0$), overall decreasing the field in the outer medium, and consequently the modal losses.

By focusing exclusively on the cladding, a key advantage of the reflection-based model is the ability to decipher the underlying physical mechanics of the light reflection process of the microstructure, which can be difficult in full numerical mode simulations. This principally allows investigating sophisticated concepts from fields such as photonic crystals (e.g., far-field cancellation [36] or Q-factor engineering [37]) or nanophotonics-related effects (e.g., bound states in the continuum [38] or Kerker effect [39,40]) within the context of low-loss guidance leaky waveguides.

Another advantage of the reflection-based model is the greatly reduced computational effort, which becomes relevant especially for large-core microstructured fibers and waveguides. Based on the complex reflection coefficients, which can be determined from straightforward numerical simulations, both dispersion and loss of the fundamental mode can be quantitatively analyzed with an analytical equation in a simple and efficient way. Note that the model is not restricted to the FM and also higher-order modes can also be investigated in a similar way ((an analysis of the lowest order HOMs (TE_{01} and TM_{01} modes) is shown in the Supplement 1 (dispersions of phase indices and modal losses are shown in Fig. S1)).

From the geometry perspective, the model is not limited to single ring structures such as light cages [3,41], and can principally be extended to other cladding structures, as long as the assumptions made for the model's derivation are valid. This in particular includes the assumptions that (i) the core diameter must be significantly larger than the wavelength ($D \gg \lambda$), and (ii) the thickness of the microstructured cladding must be small compared to the core radius. Note that a structure with considerably higher RI contrast requires an analysis of TE- and TM-reflection separately to obtain the results for the HE_{11} mode, as discussed in one of our previous works [32]. The characteristic features of the model to dominantly concentrate on the cladding suggest that it might be useful within the context of lowering losses in currently investigated hollow-core fibers (e.g., anti-resonant fibers [42–44] or Omniguides [45]). The validity and applicability of the planar reflection model in relation to other waveguides represents the next step in the analysis and is currently being intensively pursued in our research team.

5. Conclusion

Waveguides with a low refractive index core represent a promising class of integrated photonic devices and require a detailed understanding of the cladding properties due to the specifics of the light guiding process. In this work, we have introduced a quasi-analytic model that allows to study mode formation in such waveguides through solely focusing on the characteristics of the microstructured cladding. The model separates the reflection properties of the cladding from the modes by introducing equations that correlate the complex amplitude reflection coefficient of the cladding to the complex effective index of the fundamental core mode. The relevance of the model was demonstrated by analyzing mode formation in all-solid single-ring anti-resonant fibers, confirming the validity of the model. Additionally, we introduce the relative phase between forward scattered and incident fields as the key parameter for reducing loss in microstructured waveguides. By conducting extensive parameter sweeps, unexpected situations of exceptionally low loss were found for specific combinations of geometric parameters, particularly in cases the cylinders have alternating diameters.

Overall, our model, which also holds for higher-order modes, allows interpreting light guidance in microstructured low refractive index core waveguides from a scattering perspective. In contrast to a modal analysis, light scattering provides intuitive insights into the underlying physics by focusing solely on the cladding properties, while additionally allowing for extensive parameter sweeps on reasonable time scales. Here, we believe that our approach can serve as a bridge between waveguide modes and known concepts from other areas of photonics, e.g., regarding metamaterials or photonic crystals, or even cutting-edge topics such as bounded states in the continuum. Therefore, our model represents a unique platform for the introduction and investigation of previously unused optical effects in the context of fiber and waveguide optics, with the overarching goal of developing novel waveguides with unprecedented properties.

In a future step, we plan to implement a corresponding fiber using for instance the stack-and-draw approach and to compare the discussed simulated results with experimental data in order to prove the specific guiding properties of the single-ring structure and to verify the model. In addition, the applicability of the model to other waveguide structures such as hollow core fibers or Omniguides will be investigated in a study to be published in the future.

Funding. Deutsche Forschungsgemeinschaft (SCHM2655/11-1, SCHM2655/15-1, SCHM2655/8-1).

Acknowledgments. We acknowledge support by the German Research Foundation and the Open Access Publication Fund of the Thueringer Universitaets- und Landesbibliothek Jena Projekt-Nr. 433052568.

Disclosures. The authors declare no conflicts of interest.

Optics EXPRESS

Data availability. Data underlying the results presented in this paper are not publicly available at this time but may be obtained from the authors upon reasonable request.

Supplemental document. See Supplement 1 for supporting content.

References

1. M. Nissen, B. Doherty, J. Hamperl, J. Kobelke, K. Weber, T. Henkel, and M. A. Schmidt, "Uv absorption spectroscopy in water-filled antiresonant hollow core fibers for pharmaceutical detection," Sensors **18**(2), 478 (2018).
2. R. Sollapur, D. Kartashov, M. Zürch, A. Hoffmann, T. Grigorova, G. Sauer, A. Hartung, A. Schwuchow, J. Bierlich, J. Kobelke, and M. Chemnitz, "Resonance-enhanced multi-octave supercontinuum generation in antiresonant hollow-core fibers," Light: Sci. Appl. **6**(12), e17124 (2017).
3. F. Davidson-Marquis, J. Gargiulo, E. Gómez-López, B. Jang, T. Kroh, C. Müller, M. Ziegler, S. A. Maier, H. Kübler, M. A. Schmidt, and O. Benson, "Coherent interaction of atoms with a beam of light confined in a light cage," Light: Sci. Appl. **10**(1), 114 (2021).
4. J. Hu and C. R. Menyuk, "Understanding leaky modes: slab waveguide revisited," Adv. Opt. Photonics **1**(1), 58–106 (2009).
5. M. Ibanescu, Y. Fink, S. Fan, E. L. Thomas, and J. D. Joannopoulos, "An all-dielectric coaxial waveguide," Science **289**(5478), 415–419 (2000).
6. N. Litchinitser, A. Abeeluck, C. Headley, and B. Eggleton, "Antiresonant reflecting photonic crystal optical waveguides," Opt. Lett. **27**(18), 1592–1594 (2002).
7. R. Cregan, B. Mangan, J. Knight, T. Birks, P. S. J. Russell, P. Roberts, and D. Allan, "Single-mode photonic band gap guidance of light in air," Science **285**(5433), 1537–1539 (1999).
8. C. M. Smith, N. Venkataraman, M. T. Gallagher, D. Müller, J. A. West, N. F. Borrelli, D. C. Allan, and K. W. Koch, "Low-loss hollow-core silica/air photonic bandgap fibre," Nature **424**(6949), 657–659 (2003).
9. F. Couny, F. Benabid, and P. Light, "Large-pitch kagome-structured hollow-core photonic crystal fiber," Opt. Lett. **31**(24), 3574–3576 (2006).
10. Y. Wang, N. V. Wheeler, F. Couny, P. Roberts, and F. Benabid, "Low loss broadband transmission in hypocycloid-core kagome hollow-core photonic crystal fiber," Opt. Lett. **36**(5), 669–671 (2011).
11. T. Birks, F. Luan, G. Pearce, A. Wang, J. Knight, and D. Bird, "Bend loss in all-solid bandgap fibres," Opt. Express **14**(12), 5688–5698 (2006).
12. M. A. Schmidt, N. Granzow, N. Da, M. Peng, L. Wondraczek, and P. S. J. Russell, "All-solid bandgap guiding in tellurite-filled silica photonic crystal fibers," Opt. Lett. **34**(13), 1946–1948 (2009).
13. N. Granzow, P. Uebel, M. A. Schmidt, A. S. Tverjanovich, L. Wondraczek, and P. S. J. Russell, "Bandgap guidance in hybrid chalcogenide–silica photonic crystal fibers," Opt. Lett. **36**(13), 2432–2434 (2011).
14. J.-P. Yehouessi, O. Vanvincq, A. Cassez, M. Douay, Y. Quiquempois, G. Bouwmans, and L. Bigot, "Extreme large mode area in single-mode pixelated bragg fiber," Opt. Express **24**(5), 4761–4770 (2016).
15. X. Zhu, D. Wu, Y. Wang, F. Yu, Q. Li, Y. Qi, J. Knight, S. Chen, and L. Hu, "Delivery of cw laser power up to 300 watts at 1080 nm by an uncooled low-loss anti-resonant hollow-core fiber," Opt. Express **29**(2), 1492–1501 (2021).
16. B. Jang, J. Gargiulo, J. Kim, J. Bürger, S. Both, H. Lehmann, T. Wieduwilt, T. Weiss, S. A. Maier, and M. A. Schmidt, "Fiber-integrated hollow-core light cage for gas spectroscopy," APL Photonics **6**(6), 061301 (2021).
17. J.-L. Archambault, R. J. Black, S. Lacroix, and J. Bures, "Loss calculations for antiresonant waveguides," J. Lightwave Technol. **11**(3), 416–423 (1993).
18. D. Bird, "Attenuation of model hollow-core, anti-resonant fibres," Opt. Express **25**(19), 23215–23237 (2017).
19. W. Ding and Y. Wang, "Analytic model for light guidance in single-wall hollow-core anti-resonant fibers," Opt. Express **22**(22), 27242–27256 (2014).
20. M. Finger, N. Joly, T. Weiss, and P. S. J. Russell, "Accuracy of the capillary approximation for gas-filled kagomé-style photonic crystal fibers," Opt. Lett. **39**(4), 821–824 (2014).
21. M. Zeisberger and M. A. Schmidt, "Analytic model for the complex effective index of the leaky modes of tube-type anti-resonant hollow core fibers," Sci. Rep. **7**(1), 11761 (2017).
22. Y. Wang and W. Ding, "Confinement loss in hollow-core negative curvature fiber: A multi-layered model," Opt. Express **25**(26), 33122–33133 (2017).
23. P. Song, K. Y. Phoong, and D. Bird, "Quantitative analysis of anti-resonance in single-ring, hollow-core fibres," Opt. Express **27**(20), 27745–27760 (2019).
24. M. Bache, M. S. Habib, C. Markos, and J. Lægsgaard, "Poor-man's model of hollow-core anti-resonant fibers," J. Opt. Soc. Am. B **36**(1), 69–80 (2019).
25. N. M. Litchinitser, S. C. Dunn, B. Usner, B. J. Eggleton, T. P. White, R. C. McPhedran, and C. M. de Sterke, "Resonances in microstructured optical waveguides," Opt. Express **11**(10), 1243–1251 (2003).
26. T. A. Birks, G. J. Pearce, and D. M. Bird, "Approximate band structure calculation for photonic bandgap fibres," Opt. Express **14**(20), 9483–9490 (2006).
27. G. Li and M. A. Schmidt, "Identification of zero density of states domains in band gap fibers using a single binary function," Opt. Express **24**(14), 16212–16221 (2016).
28. R. F. Ando, A. Hartung, B. Jang, and M. A. Schmidt, "Approximate model for analyzing band structures of single-ring hollow-core anti-resonant fibers," Opt. Express **27**(7), 10009–10021 (2019).
29. A. W. Snyder and J. Love, *Optical waveguide theory* (Springer Science & Business Media, 2012).

Optics EXPRESS

30. E. Istrate and E. H. Sargent, "Photonic crystal waveguide analysis using interface boundary conditions," IEEE J. Quantum Electron. **41**(3), 461–467 (2005).
31. P. Blown, C. Fisher, F. J. Lawrence, N. Gutman, and C. M. de Sterke, "Semi-analytic method for slow light photonic crystal waveguide design," Photonics Nanostructures - Fundam. Appl. **10**(4), 478–484 (2012).
32. G. Li, M. Zeisberger, and M. A. Schmidt, "Guiding light in a water core all-solid cladding photonic band gap fiber–an innovative platform for fiber-based optofluidics," Opt. Express **25**(19), 22467–22479 (2017).
33. I. H. Malitson, "Interspecimen comparison of the refractive index of fused silica," J. Opt. Soc. Am. **55**(10), 1205–1209 (1965).
34. A. Argyros, T. Birks, S. Leon-Saval, C. Cordeiro, F. Luan, and P. S. J. Russell, "Photonic bandgap with an index step of one percent," Opt. Express **13**(1), 309–314 (2005).
35. S. Upendar, R. Ando, M. Schmidt, and T. Weiss, "Orders of magnitude loss reduction in photonic bandgap fibers by engineering the core surround," Opt. Express **29**(6), 8606–8616 (2021).
36. S.-H. Kim, J. Huang, and A. Scherer, "Photonic crystal nanocavity laser in an optically very thick slab," Opt. Lett. **37**(4), 488–490 (2012).
37. G. Böttger, M. Schmidt, M. Eich, R. Boucher, and U. Hübner, "Photonic crystal all-polymer slab resonators," J. Appl. Phys. **98**(10), 103101 (2005).
38. K. Koshelev, A. Bogdanov, and Y. Kivshar, "Engineering with bound states in the continuum," Opt. Photonics News **31**(1), 38–45 (2020).
39. A. F. Cihan, A. G. Curto, S. Raza, P. G. Kik, and M. L. Brongersma, "Silicon mie resonators for highly directional light emission from monolayer mos 2," Nat. Photonics **12**(5), 284–290 (2018).
40. A. Vaskin, J. Bohn, K. E. Chong, T. Bucher, M. Zilk, D.-Y. Choi, D. N. Neshev, Y. S. Kivshar, T. Pertsch, and I. Staude, "Directional and spectral shaping of light emission with mie-resonant silicon nanoantenna arrays," ACS Photonics **5**(4), 1359–1364 (2018).
41. C. Jain, A. Braun, J. Gargiulo, B. Jang, G. Li, H. Lehmann, S. A. Maier, and M. A. Schmidt, "Hollow core light cage: trapping light behind bars," ACS Photonics **6**(3), 649–658 (2019).
42. P. Roberts, D. Williams, B. Mangan, H. Sabert, F. Couny, W. Wadsworth, T. Birks, J. Knight, and P. S. J. Russell, "Realizing low loss air core photonic crystal fibers by exploiting an antiresonant core surround," Opt. Express **13**(20), 8277–8285 (2005).
43. A. Hartung, J. Kobelke, A. Schwuchow, K. Wondraczek, J. Bierlich, J. Popp, T. Frosch, and M. A. Schmidt, "Double antiresonant hollow core fiber–guidance in the deep ultraviolet by modified tunneling leaky modes," Opt. Express **22**(16), 19131–19140 (2014).
44. M. S. Habib, J. Antonio-Lopez, C. Markos, A. Schülzgen, and R. Amezcua-Correa, "Single-mode, low loss hollow-core anti-resonant fiber designs," Opt. Express **27**(4), 3824–3836 (2019).
45. B. Temelkuran, S. D. Hart, G. Benoit, J. D. Joannopoulos, and Y. Fink, "Wavelength-scalable hollow optical fibres with large photonic bandgaps for co 2 laser transmission," Nature **420**(6916), 650–653 (2002).